Journal of Alloys and Compounds 1014 (2025) 178787

Contents lists available at ScienceDirect

Journal of Alloys and Compounds

journal homepage: www.elsevier.com/locate/jalcom

Effect of thickness and halide composition on the resistive switching and photonic synapse properties of methylammonium lead bromide thin films

Won Chang Choi [a,1], Yeonghun Yun [b,1], SangMyeong Lee [c], Yunmo Kang [a], Hyun Suk Jung [c,d], In Sun Cho [e,*], Sangwook Lee [a,*]

[a] School of Materials Science and Engineering, Kyungpook National University, Daegu 41566, Republic of Korea
[b] Department Perovskite Tandem Solar Cells, Helmholtz-Zentrum Berlin für Materialien und Energie GmbH, Berlin 12489, Germany
[c] School of Advanced Materials Science & Engineering, Sungkyunkwan University, Suwon 16419, Republic of Korea
[d] SKKU Institute of Energy Science and Technology (SIEST), Sungkyunkwan University, Suwon 16419, Republic of Korea
[e] Department of Materials Science and Engineering, and Energy Systems Research, Ajou University, Suwon 16499, Republic of Korea

ARTICLE INFO

Keywords:
Halide perovskites
Photonic synapse
Resistive switching
Film thickness
Chlorine substitution

ABSTRACT

Recently, photonic synapses based on halide perovskite resistive switching devices have been intensively studied due to their low power consumption, high information processing speed, and the ability to simultaneously receive optical and electrical signals. In this study, the resistive switching behavior and photo-synaptic properties of methylammonium lead bromide ($MAPbBr_3$) thin films were investigated by varying thicknesses and substituting bromine with chlorine. The thickest film (330 nm) exhibits a single step of resistive switching from a high resistance state to a low resistance state (SET), which is attributed to the formation of conductive filaments by the migration of halide vacancies. In contrast, thinner films (100 nm and 210 nm) show two steps of SET where both the halide vacancies and electrode ions (Ag^+) are involved in the formation of conductive filaments. Among the films, the 210 nm-thick film exhibited the most effective potentiation by repeated light exposure. When incorporating Cl into the $MAPbBr_3$ film, the resistive switching voltages and the light-induced potentiation was decreased. This was attributed to the smaller ion size of Cl compared to Br, which facilitates ion migration and the formation of vacancy filaments. Short-term potentiation and long-term depression under light pulses were characterized using paired-pulse facilitation and paired-pulse depression.

1. Introduction

The Von Neumann architecture, a conventional framework for information processing systems, requires rapid processing capabilities, real-time information handling, and efficient power consumption to manage extensive data loads and the Internet of Things (IoT) [1–3]. However, the architecture's inherent separation of the information processing unit from the memory unit creates a bottleneck due to the speed difference between information processing and memory unit data transmission [4,5]. The human brain, a remarkable biological system, consists of approximately 10^{12} neurons interconnected through an intricate neural network. Each neuron connects with over 1000 synapses, facilitating information transmission to neighboring neurons [6,7]. This intricate neural architecture enables the brain to transfer information efficiently while consuming remarkably low amounts of energy, typically ranging from 1 to 100 fJ per synaptic transmission [8,9]. As a result, there is significant interest in replicating the brain's functionality within artificial intelligence devices [10].

For humans, more than 80 % of information about the external environment is obtained from visual information [11,12]. Photonic synapses with high bandwidth, high light sensitivity, and low power consumption are crucial for the development of artificial visual response systems [13–15]. With the continuous advancement of artificial photonic synapses developed using diverse materials and strategies, their performance has significantly enhanced. Accordingly, energy consumption levels have approached that of the human brain, approximately ~10 fJ per synaptic event [16–18]. This implies a significant potential reduction of power consumption in artificial intelligence computations compared to the current complementary metal-oxide semiconductor (CMOS)-based neuromorphic systems, which consumes

* Corresponding authors.
E-mail addresses: insuncho@ajou.ac.kr (I.S. Cho), wook2@knu.ac.kr (S. Lee).
[1] Equally contributed.

https://doi.org/10.1016/j.jallcom.2025.178787
Received 28 August 2024; Received in revised form 22 November 2024; Accepted 20 January 2025
Available online 21 January 2025

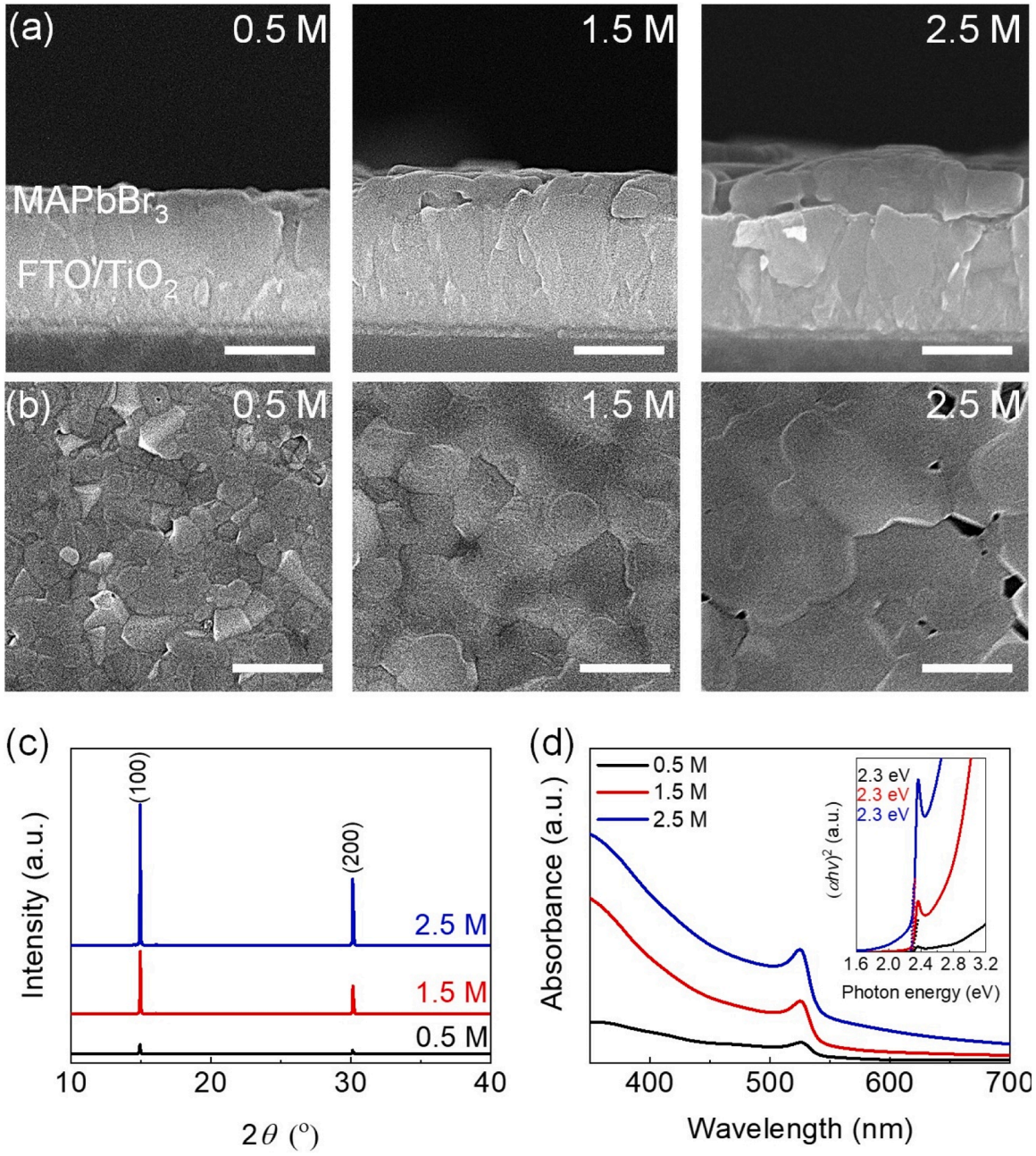

Fig. 1. Properties of the perovskite films with varying precursor solution concentrations: (a) cross-sectional SEM images (scale bar: 500 nm), (b) plane-view SEM images (scale bar: 500 nm), (c) XRD patterns, and (d) absorbance spectrum with Tauc plot inserted.

tens to hundreds of pJ per synaptic event [19]. One of the problems in developing photonic synapses is photoactive layer material which transforms applied optical signals to electrical signals [20]. Halide perovskites are highly promising materials for the photonic synapse systems due to their exceptional optical and electrical characteristics, including a high light absorption coefficient, facile bandgap tunability, small exciton binding energy, and long carrier diffusion length [21,22]. In 2016, perovskite synaptic devices based on polycrystalline methylammonium lead iodide ($MAPbI_3$) were first developed [23]. In addition, perovskite-based photonic synapses with different compositions, including $CsPbBr_3$ [12,24], $CsPb(Br_{1-x}I_x)_3$ [25], $CsPbCl_3$ [26], $(PEA)_2SnI_4$ [27], $Cs_3Sb_2Br_9$ [28], $Cs_2AgBiBr_6$ [29], and BA_2PbBr_4 [30], (where PEA and BA are phenethylammonium and butylammonium, respectively) have been studied. $MAPbBr_3$-based photonic synapses have been widely studied, since $MAPbBr_3$-based synaptic device was firstly implemented by synthesizing a $MAPbBr_3$ thin film on top of a buffer-capped conducting polymer [16]. this research has reported the mechanism of synaptic behavior involving bromine ions and vacancies. An ON/OFF ratio of 10^6 and a low SET voltage of −0.2 V were achieved using a $MAPbBr_3$ thin film composed of nanoparticles, and the mechanism of conducting filament formation through bromine vacancy movement by an external electric field was identified [31].

In this study, we investigated the resistive switching behavior and photo-synaptic properties of $MAPbBr_3$ thin films with varying thicknesses and by substituting bromine with chlorine. The thickness of the perovskite film was controlled by varying the concentration of perovskite precursor solution. The Cl ions were incorporated into the perovskite precursor to substitute the Br ions, evidenced by decreased lattice parameters of the perovskite films. The changes in the resistive switching behavior and photo-synaptic properties were systematically

studied in relation to the conductive filament formation by halide vacancy or electrode metal ions, influenced by film thickness and halide mixing. In addition, short-term potentiation and long-term depression under light pulses were characterized by modulating the light pulse intervals.

2. Materials and methods

2.1. Materials

Methylammonium bromide (MABr, >99.99 %) and methylammonium chloride (MACl, >99.99 %) were purchased from Great Cell Solar Materials. Lead bromide ($PbBr_2$, >98 %) and lead chloride ($PbCl_2$, >99.5 %) were purchased from Tokyo Chemical Industries. Titanium diisopropoxide bis(acetylacetonate) (TDIP, 75 % in 2-propanol), 1-butanol (99.9 %), dimethyl sulfoxide (DMSO, >99.9 %, anhydrous), and diethyl ether (DEE, 99.8 %, anhydrous) were purchased from Sigma-Aldrich.

2.2. Fabrication of $MAPbBr_3$–based synaptic devices

Fluorine-doped tin oxide (FTO, Pilkington TEC7, 7 Ω) substrates were cleaned by ultrasonication with acetone, distilled water, and ethanol, each for 5 min. The cleaned substrates were dried under a nitrogen gas, followed by UV-O_3 plasma treatment for 30 min. 50 nm-thick TiO_2 layer was deposited on the FTO substrate by spin-coating a TDIP solution (50 μL), with 3000 rpm for 20 seconds. The TDIP solution was prepared by adding 74 μL of TDIP to 926 μL of 1-butanol, followed by stirring for 12 h. The TDIP-coated FTO substrates were annealed at 125°C for 5 min and 500°C for 30 min. $MAPbBr_3$ precursor solutions were prepared in three distinct concentrations: 0.5 M, 1.5 M, and 2.5 M, by dissolving MABr and $PbBr_2$ in DMSO. For the MAPb(Br-Cl)$_3$ thin films, the stoichiometric amount of MACl and $PbCl_2$ were added to the precursor solution. The precursors were spin-coated on the TiO_2-coated FTO substrates, at 4000 rpm for 20 s. At the 9 s, 0.5 ml of DEE was dispensed onto the spinning substrate. Following the spin-coating procedure, the coated perovskite thin films were sequentially annealed at 65°C and 100°C for 1 min and 2 min, respectively. Finally, a 100 nm-thick Ag electrode was deposited onto the perovskite film using a thermal evaporator. The active area of the photo-synaptic device was 0.332 cm^2.

2.3. Characterizations and device measurements

Crystallographic structural properties of the perovskite films were examined by X-ray diffraction (XRD, X'Pert Powder, PANalytical) with Cu Kα rays. Absorbance spectra were acquired using UV–vis–NIR spectroscopy (Cary 5000, Agilent Technologies). A field emission-scanning electron microscope (FE-SEM, JSM-6701F, JEOL) was used to observe the top-view and cross-sectional microstructures of the perovskite films. The electrical properties of the perovskite devices were characterized using a semiconductor parameter analyzer (4200-SCS, Keithley). The optoelectronic responses of the devices were collected under light pulses from a diode laser (MD4050, Delos Laser).

3. Results and discussion

The commonly employed device structure consists of a vertical sandwich configuration comprising metal-insulator-metal layers [32], where Ag serves as the upper layer, while FTO is utilized as the lower electrode [32]. In such systems, in many cases, the rough surface of the FTO substrate leads to non-uniformity in the deposition of the $MAPbBr_3$ thin film [33,34], resulting in numerous pinholes that expose the underlying FTO layer (Fig. S1(a, b)). The linear current-voltage (*I-V*) curve and consistent device resistance depicted in Fig. S2 indicate ohmic contact, mimicking the behavior of a metal-metal interface [35]. To address this issue, an n-type oxide layer, TiO_2, was introduced to prevent direct contact between the silver and FTO electrodes, thereby preventing ohmic contact. Additionally, TiO_2 is known for its super-hydrophilic properties [33], facilitating the easy spreading of the perovskite precursor solution, particularly when using hydrophilic solvents. This characteristic promotes even coating of the perovskite layer on the substrate, facilitating the formation of high-quality perovskite thin films [34]. Therefore, the introduction of TiO_2 layer would also improve the

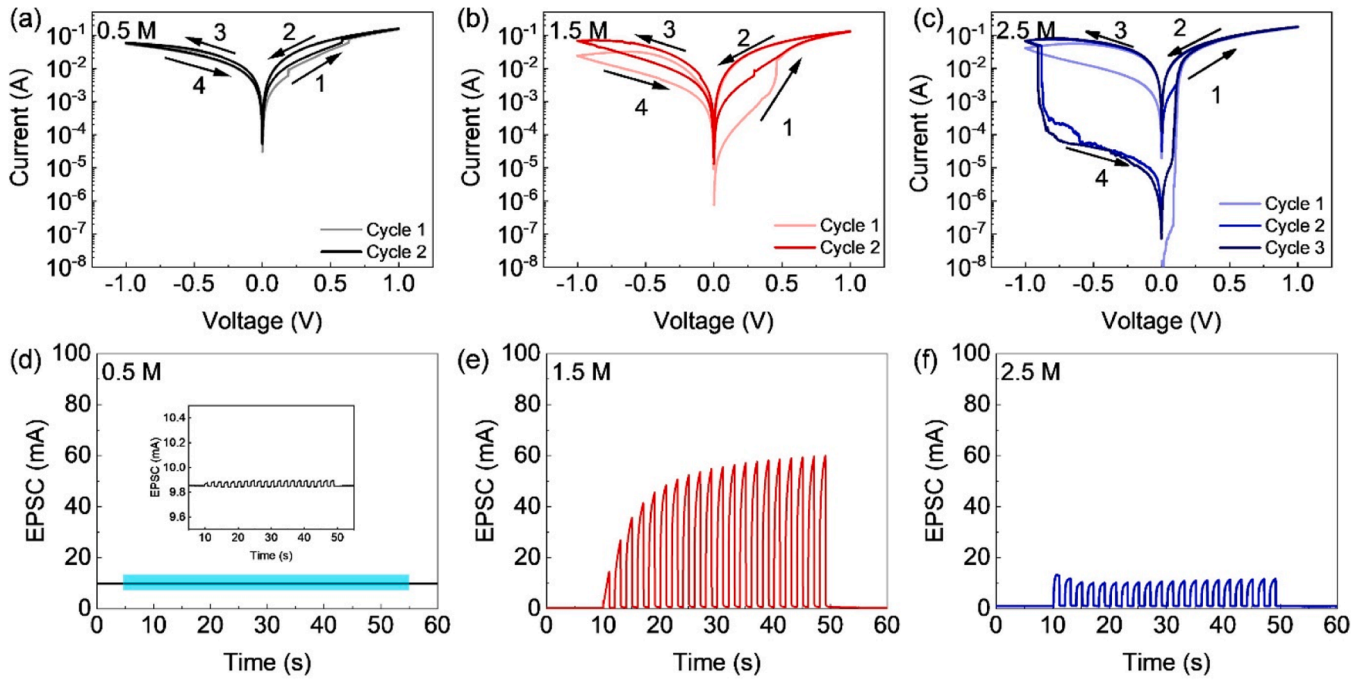

Fig. 2. Properties of the synaptic devices made from thin films, (a, d) 0.5 M, (b, e) 1.5 M, and (c, f) 2.5 M. (a-c) *I-V* characteristics at a sweeping rate of 0.1 V s^{-1} under dark conditions. (d-f) EPSC excited by 20 photonic pulses with an intensity of 12 mW cm^{-2} and a duration of 1 s (light wavelength: 450 nm), under the applied voltage of −0.02 V.

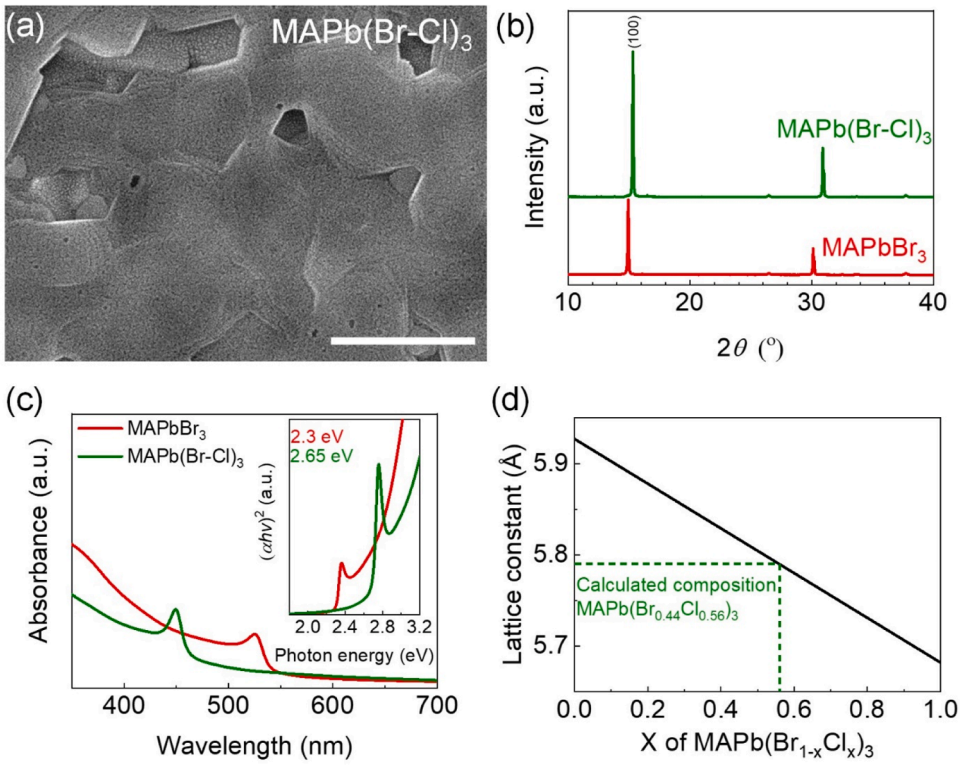

Fig. 3. (a) SEM images (scale bar: 500 nm) of the $MAPb(Br\text{-}Cl)_3$ film (b) XRD pattern of $MAPbBr_3$ and $MAPb(Br\text{-}Cl)_3$ films. (c) Absorbance spectrum $MAPbBr_3$ and $MAPb(Br\text{-}Cl)_3$ films with Tauc plot. (d) Optical bandgap and lattice constant of the $MAPb(Br_{1-x}Cl_x)_3$ composition based on Vegard's law. The real composition of our $MAPb(Br\text{-}Cl)_3$ thin film was obtained using experimentally secured bandgap and lattice constant.

photoresponse of our devices because of the improved perovskite morphology, and well-known advantageous of TiO_2 as a charge trasnport or injection layer [36].

We successfully synthesized perovskite thin films of various thicknesses on FTO/TiO_2 layers, using precursor solutions with concentrations of 0.5 M, 1.5 M, and 2.5 M. The thicknesses were determined via cross-sectional SEM analysis and are depicted in Fig. 1(a), measuring 100 nm, 210 nm, and 330 nm, respectively. The grain size of films increases with the concentration of precursor solution, as shown in the plane-view SEM images in Fig. 1(b). Notably, perovskite film based on 2.5 M solution showed pin-holes, which can be formed due to the evaporation of residual DMSO during the annealing [37]. It is known that the pin-holes in perovskite films can play a crucial role of defect generation and/or migration [38]. To verify the successful synthesis of the films as $MAPbBr_3$, XRD analysis was conducted, as presented in Fig. 1(c). From the results, all synthesized films were comprised of $MAPbBr_3$, with a preferred orientation along the (100) plane [39]. The intensity of the diffraction peaks increased with film thickness. To investigate the optical characteristics of the synthesized thin films, we measured their absorbance spectra, as depicted in Fig. 1(d), revealing that the films exhibit band-to-band transition absorption up to a wavelength of ~550 nm, with an exciton-derived absorption peak at approximately 525 nm that corresponds to previous reports [40]. Additionally, the absorbance intensity of thin films increases linearly with film thickness without unexpected changes due to reflectance or scattering. The inset of Fig. 1(d) is a graph derived from the Tauc plot [39], utilized to ascertain the optical bandgap of the films. The calculated optical bandgaps of these thin films are approximately 2.3 eV, aligning with the previously reported bandgap for $MAPbBr_3$ [39]. This consistency in the optical bandgap across different thicknesses underscores the reproducible optical properties of the thin films, further highlighting their potential for applications requiring precise optical characteristics.

A synaptic device was fabricated based on the aforementioned perovskite films with the FTO/TiO_2/perovskite/Ag configuration. In this configuration of synaptic devices based on perovskites, it has been reported that SET and RESET occur by two primary mechanisms:[41] the electrochemical metallization mechanism (ECM) driven by the infiltration of electrode ions and the valence change mechanism (VCM) facilitated by the migration of halide ions. In ECM, when a positive voltage is applied to the top electrode, electrode ions infiltrate the perovskite due to the external electric field, forming conducting filaments that lead to SET behavior when these filaments interact with the bottom electrode. Conversely, applying a voltage in the opposite direction causes the electrode ions to move in the opposite direction due to the electric field, resulting in the interruption of filaments and RESET behavior. In VCM, halide ions accumulate on the bottom electrode when a negative voltage is applied, leading to filament formation and SET behavior. Applying a negative voltage to the top electrode causes the accumulated ions to detach, triggering RESET behavior. Therefore, our devices were expected to exhibit both ECM and VCM behaviors, as observed in previous studies involving halide perovskite [41].

In Fig. 2(a-c), we presented the *I-V* curves of our devices for two cycles of voltage sweep of $0 \rightarrow 1 \rightarrow 0 \rightarrow -1$ V in ambient air. Our devices reveal electroforming process in the first cycle, which promotes the significant change in the conductance and stabilize the resistive switching [42,43]. In the second cycle, all tested devices exhibit stabilized resistive switching upon voltage sweep. To make it more clarified, we presented *I–V* characteristics up to cycle 3 for 2.5 M device. They show SET behavior, transitioning from a high resistance state (HRS) to a low resistance state (LRS) when a voltage of $0 \rightarrow 1$ V is applied. They maintain LRS upon the voltage of $1 \rightarrow 0 \rightarrow -1$ V. Next, they display RESET behavior, reverting to a HRS when the negative voltage is switched from $-1 \rightarrow 0$ V. However, notable differences in the voltage thresholds and profiles of the SET and RESET behaviors are observed among the samples. SET steps and corresponding threshold voltages

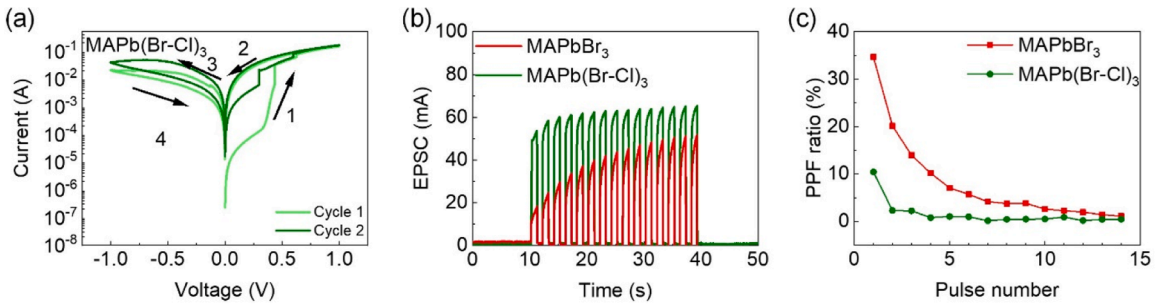

Fig. 4. Synaptic properties of device based on the $MAPbBr_3$ and $MAPb(Br\text{-}Cl)_3$ films: (a) *I-V* characteristics of $MAPb(Br\text{-}Cl)_3$-based device at a sweeping rate of 0.1 V s^{-1} under a dark condition, (b) EPSC excited by 15 photonic pulse with an intensity of 12 mW cm^{-2} and duration of 1 s (light wavelength: 450 nm), under the applied voltage of −0.02 V, and (c) PPF ratio calculated from (b).

were different. 2.5 M device exhibited just one step of SET at a relatively low voltage (0.1 V), while 0.5 M, and 1.5 M device showed two steps of SET at both the low (0.25–0.3 V) and high voltage (~0.6 V), respectively. It has been reported that filament formation by the halide vacancies induces a lower voltage SET around 0.25 V, while filament formation by Ag electrodes leads to a higher voltage SET around 0.56 V [41]. Therefore, from now on, we will refer to SET at the low voltages as SET_{Vx} and the high voltages as SET_{Ag}. It can be seen that filaments by halide vacancies were formed in all three films. Relatively premature SET_{Vx} of 2.5 M device is thought to be caused by the pin-holes in the film, which provide a facile path for material diffusion and potentially possess a high concentration of defects, as described above. The absence of SET_{Ag} in the 2.5 M device suggests that the migration of Ag ions to form a filament could be impeded due to the thick film, implying that SET_{Ag} might be observable under higher voltage. We note that the migration of Ag ions is slower than that of halide ions/vacancies, resulting in the destruction of the halide vacancy filaments prior to Ag filaments, consequently single-step RESET behavior, consistent with the literature [41]. It is also worth noting that the magnitude of resistance change induced by Ag ions is smaller than that expected for a pure Ag-based system likely because the resistance switching caused by Ag ions occurs after switching induced by halide vacancies as previously reported [41,44]. For a further in-depth analysis, we looked into the *I-V* characteristics of 0.5 M device in log-log scale (Fig. S3). It was observed that the first SET process follows a space-charge limited current (SCLC) mechanism [45] as previously demonstrated [45]. The *I-V* curve showed obvious ohmic (m_1), trap-limited SCLC (m_2), trap-filled limit (m_3), and trap-free SCLC (m_4 and m_5) regions. On the other hand, m_5 is much steeper than m_4, which implies that there is another source decreasing the resistance of the perovskite film. Considering the steep slope of m_5, the current jump at a high voltage of ~ 0.6 V (different from the low voltage SET), and the very low resistance (~8.69 Ω) and slope (~1.6) after the jump, we attribute the second jump as the second SET by the formation of Ag filament with Schottky junction, consistently with literature [41,46–48]. We propose that a film made using the 1.5 M solution represents an optimal thickness, as it shows the most significant resistance potentiation upon the repeated voltage sweep. This result implies that the SET mechanism of a perovskite-based device can be adjusted by the thickness of the perovskite film.

Furthermore, we evaluated excitatory postsynaptic current (EPSC) in response to light for each device (Fig. 2(d-f)). EPSC is derived from excitatory postsynaptic potentials (EPSPs), which temporarily elevate the membrane potential, increasing the likelihood of neuron activation upon external stimulation. In our devices, the formation of filaments in response to external light pulses temporarily decreases the resistance, thereby manifesting the potentiation phenomenon [41]. For the 1.5 M device, the light induced photo-current was observed to increase up to 60 mA with the repeated light stimulation, indicating a reinforcing effect (Fig. 2(e)). However, the devices with 0.5 and 2.5 M show negligible change in photo-current with the repeated light stimulation (Fig. 2(d-f)), likely due to the hardly changing filament upon repeated stimulation, attributed to the thin film thickness and defective film, respectively. The 1.5 M solution concentration is taken as the optimal balance, showing the best properties when voltage-induced synaptic behavior and light-induced synaptic behavior are considered together, and the 210 nm thin film fabricated using this solution is considered the optimal thickness. We compared our device's properties with those of other devices reported, in Table S1.

In Fig. 3(a), a plane-view SEM image of the $MAPb(Br\text{-}Cl)_3$ thin film, controlled to have a thickness of 210 nm, is presented, revealing that the film exhibits an uniform appearance akin to its undoped counterpart. However, the grain size of $MAPb(Br\text{-}Cl)_3$ thin film is notably larger compared to $MAPbBr_3$. The increase in grain size observed upon Cl-substitution is due to the fact that the $MAPb(Br\text{-}Cl)_3$ composition is a thermodynamically more stable phase, has a lower formation energy compared to $MAPbBr_3$, and Cl ions diffuse from within the grains into the grains [49]. XRD analysis was conducted to confirm the successful synthesis of both thin films as a $MAPbBr_3$ perovskite. As depicted in Fig. 3(b), the analysis demonstrates that the synthesized thin films are indeed $MAPbBr_3$ perovskite [39]. Furthermore, the XRD patterns indicate a predominant orientation of both thin films toward the (100) plane. Comparing the $MAPbBr_3$ and $MAPb(Br\text{-}Cl)_3$ thin films, an increase in XRD intensity with larger grain size is observed, indicating improved crystallinity with increasing grain size [50]. Notably, the XRD peak of the $MAPb(Br\text{-}Cl)_3$ thin film shifted to a higher angle (Fig. S4). Absorbance spectra with Tauc plot results indicate the shift of bandgap from 2.3 eV to 2.65 eV (Fig. 3(c)). This is caused by the presence of Cl in the film, which not only contributes to crystal growth but also infiltrates the perovskite structure. The smaller ionic radius of Cl (181 pm) compared to Br (196 pm) leads to lattice contraction, shifting the XRD peak to a higher angle [50]. Since the lattice parameters of halide perovskite follow well the Vegard's law, the composition of the thin film was determined using the (001) interplanar distance [39,51]. The a-lattice parameter of the $MAPbBr_3$ and that of $MAPb(Br\text{-}Cl)_3$ thin film was determined to be 5.93 Å and 5.79 Å, respectively, consistent with the lattice parameters in the reported paper [39,52]. Considering the lattice parameter, the actual composition of the Cl-incorporated thin film was determined to be $MAPb(Br_{0.44}Cl_{0.56})_3$ (Fig. 3(d)).

Fig. 4(a) illustrates the resistive switching characteristics of the device based on the $MAPb(Br\text{-}Cl)_3$ film, observed during two cycles of voltage sweeping in ambient air. Similar to $MAPbBr_3$-based device shown in Fig. 2(b), Cl-incorporating device electroforming process and stabilized resistive switching behavior in the first and second voltage cycle, respectively. For $MAPbBr_3$-based device, the SET voltage occurs at 0.30 V and 0.60 V, as shown above. In contrast, $MAPb(Br\text{-}Cl)_3$-based devices exhibit SET behavior at 0.29 V and 0.59 V. The SET_{Ag} voltages are similar, while the SET_{Vx} voltage of $MAPb(Br\text{-}Cl)_3$ is lower than that of $MAPbBr_3$, which was attributed to the small size of Cl ions facilitating the diffusion and formation of filament.

The photo-responsiveness of these devices are compared in Fig. 4(b).

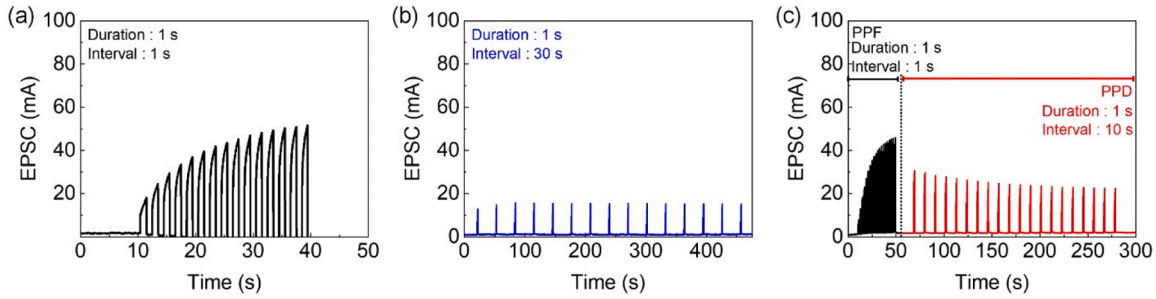

Fig. 5. Synaptic device properties based on small grain (a-b) EPSC excited by 15 photonic pulse with intensity of 12 mW cm^{-2}, duration of 1 s and interval of (a) 1 s and (b) 30 s, under the applied voltage of −0.02 V. (c) Experimental demonstration of PPD following PPF in the synaptic memory device. (450 nm, 12 mW cm^{-2}, interval changes from 1 s to 10 s).

Initially, the $MAPbBr_3$ device exhibited a lower response with a photo-current of 20 mA compared to approximately 50 mA for the $MAPb(Br-Cl)_3$ device. The lower initial photo-response of the $MAPbBr_3$ device was attributed to the higher density of the grain boundary where charge transfer would be slower than that of the grain interior [53,54]. On the other hand, after 15 light pulses, the photo-current of $MAPbBr_3$ device significantly increased by ~2.5 times, while that of $MAPb(Br-Cl)_3$ increased by only ~1.2 times. This indicates that the $MAPbBr_3$ device develops increased sensitivity to repeated stimuli, like a characteristic of synaptic behavior in short-term memory. The paired-pulse facilitation (PPF) ratios were calculated using the following formula:

$$PPF\ ratio = \quad A_2/A_1 \quad \times 100\% \tag{1}$$

where A_1 represents the current value of the device for the first light pulse, while A_2 represents the current value for the second pulse [16]. Fig. 4(c) presents PPF values calculated based on the number of light pulses, showing that PPF enhancement is more pronounced with fewer light pulses. The maximum PPF ratio for the $MAPbBr_3$ device occurs at the first pulse pair, reaching approximately 35 %. In contrast, the $MAPb(Br-Cl)_3$ device achieve a maximum PPF ratio of 10 % at the first pulse, which decreases to 0.4 % at the seventh pulses. We propose that this phenomenon is mainly attributable to the smaller grain size within the $MAPbBr_3$ thin film and/or facile migration of Cl ions in perovskite lattice. Smaller grain sizes imply a higher density of grain boundaries, where defects and halide ion vacancies, are more likely to form [55]. These conditions would inhibit the escape of photo-generated charges [56]. In other words, the higher initial photo-responsiveness of the $MAPb(Br-Cl)_3$ devices is attributed to superior charge transport in a larger grain-based film [53], due to the fewer trap sites. However, this superior charge transport character could lead to the weak strengthening effect because the photo-generated charges would dissipate more easily. Therefore, it is likely that reducing the grain size of perovskite thin films enhance the photo-synaptic characteristic. In addition, the smaller ionic radius of Cl than Br can lead to a lower activation energy and higher mobility, thereby attributing rapid destruction of filaments between external stimuli intervals due to a facile back diffusion of Cl ions. Furthermore, the rapid formation of nearly saturated density of filaments upon initial stimuli can reduce the potentiation effect, which is supposed to be observed with repeated stimulation in synapse devices. This point aligns well with previous studies, which reported that suppressing back diffusion can enhance the enhancement effect of artificial synaptic devices [57]. Therefore, it can also be recognized that there is a trade-off between ease of ion migration and the robustness of synaptic performance over multiple cycles.

Fig. 5 further confirms the photo-synaptic characteristics of the $MAPbBr_3$ device. Notably, when a light pulse is applied with one-second intervals (Fig. 5(a)), there is a gradual increase in photo-response like PPF, indicating short-term potentiation in this device. When the light application interval is extended to 30 s (Fig. 5(b)), no strengthening effect is observed, and only a consistent response to light is noted. When the pulse intervals were increased to 10 s after the saturation of EPSC with one-second intervals, the photo-current value gradually decreased like paired-pulse depression (PPD), as shown in Fig. 5(c). However, the photo-current didn't return to its original value of ~ 11 mA (the first spike by the light stimulation), indicating a long-term depression.

4. Conclusion

In this study, we investigated $MAPbBr_3$ perovskite-based photonic synapse devices to understand the effects of thin film thickness and chlorine incorporation on device performance. Our findings reveal that the SET process can be modulated by film thickness, as evidenced by a single step of SET in the thickest film (330 nm) compared to two steps of SET in the thinner films (100 nm and 210 nm). The device with a 210 nm thickness exhibited the best synaptic properties under voltage sweeps and repeated light stimulation, attributed to minimal filament strengthening in the 100 nm and 330 nm devices due to the film being too thin and the presence of pinholes, respectively. Incorporating chlorine resulted in a reduction of vacancy-induced SET voltage due to the facile diffusion and filament formation of Cl. However, the potentiation effect decreased due to the enlarged grain size. Additionally, we demonstrated the short-term potentiation and long-term depression behavior of $MAPbBr_3$-based devices under light pulses by modulating the light pulse intervals. This study shows that the synaptic properties of perovskite-based devices can be tuned by adjusting film thickness and halide content.

CRediT authorship contribution statement

Won Chang Choi: Data curation, Visualization, Investigation, Writing – original draft. **Yeonghun Yun:** Data curation, Investigation, Writing – review & editing. **SangMyeong Lee:** Investigation, **Yunmo Kang:** Investigation. **Hyun Suk Jung:** Investigation, In **Sun Cho:** Writing – review & editing. **Sangwook Lee:** Surpervision, Project administration, Conceptualization, Methodology, Writing – review & editing.

Declaration of Competing Interest

The authors declare that they have no known competing financial interests or personal relationships that could have appeared to influence the work reported in this paper.

Acknowledgements

This work was supported by the National Research Foundation of Korea (NRF, 2022M3J1A1085285, RS-2023–00302646, and 2022M3H4A1A03074093) funded by the Ministry of Science and ICT (MSIT).

Appendix A. Supporting information

Supplementary data associated with this article can be found in the online version at doi:10.1016/j.jallcom.2025.178787.

Data Availability

Data will be made available on request.

References

[1] S. Manipatruni, D.E. Nikonov, I.A. Young, Beyond CMOS computing with spin and polarization, Nat. Phys. 14 (2018) 338–343.
[2] C. Liu, X. Yan, X. Song, S. Ding, D.W. Zhang, P. Zhou, A semi-floating gate memory based on van der Waals heterostructures for quasi-non-volatile applications, Nat. Nanotechnol. 13 (2018) 404–410.
[3] P. Gkoupidenis, D.A. Koutsouras, G.G. Malliaras, Neuromorphic device architectures with global connectivity through electrolyte gating, Nat. Commun. 8 (2017) 15448.
[4] P. Yao, H. Wu, B. Gao, S.B. Eryilmaz, X. Huang, W. Zhang, Q. Zhang, N. Deng, L. Shi, H.S.P. Wong, H. Qian, Face classification using electronic synapses, Nat. Commun. 8 (2017) 15199.
[5] Z. Wang, C. Li, W. Song, M. Rao, D. Belkin, Y. Li, P. Yan, H. Jiang, P. Lin, M. Hu, J. P. Strachan, N. Ge, M. Barnell, Q. Wu, A.G. Barto, Q. Qiu, R.S. Williams, Q. Xia, J. J. Yang, Reinforcement learning with analogue memristor arrays, Nat. Electron. 2 (2019) 115–124.
[6] V.M. Ho, J.-A. Lee, K.C. Martin, The cell biology of synaptic plasticity, Science 334 (2011) 623–628.
[7] L.F. Abbott, W.G. Regehr, Synaptic computation, Nature 431 (2004) 796–803.
[8] Y. van de Burgt, E. Lubberman, E.J. Fuller, S.T. Keene, G.C. Faria, S. Agarwal, M. J. Marinella, A. Alec Talin, A. Salleo, A non-volatile organic electrochemical device as a low-voltage artificial synapse for neuromorphic computing, Nat. Mater. 16 (2017) 414–418.
[9] M.L. Schneider, C.A. Donnelly, S.E. Russek, B. Baek, M.R. Pufall, P.F. Hopkins, P.D. Dresselhaus, S.P. Benz, W.H. Rippard, Ultralow power artificial synapses using nanotextured magnetic Josephson junctions, Science Advances, 4 e1701329.
[10] S. Ullman, Using neuroscience to develop artificial intelligence, Science 363 (2019) 692–693.
[11] Q. Liu, L. Yin, C. Zhao, J. Wang, Z. Wu, H. Lei, Y. Liu, B. Tian, Z. Zhang, Z. Zhao, R. Liu, C. Ding, Y. Han, C.-Q. Ma, P. Song, I.Z. Mitrovic, E.G. Lim, Z. Wen, Hybrid mixed-dimensional perovskite/metal-oxide heterojunction for all-in-one opto-electric artificial synapse and retinal-neuromorphic system, Nano Energy 102 (2022) 107686.
[12] D. Hao, J. Zhang, S. Dai, J. Zhang, J. Huang, Perovskite/organic semiconductor-based photonic synaptic transistor for artificial visual system, ACS Appl. Mater. Interfaces 12 (2020) 39487–39495.
[13] A. Polonsky, R. Blake, J. Braun, D.J. Heeger, Neuronal activity in human primary visual cortex correlates with perception during binocular rivalry, Nat. Neurosci. 3 (2000) 1153–1159.
[14] X. Han, Z. Xu, W. Wu, X. Liu, P. Yan, C. Pan, Recent progress in optoelectronic synapses for artificial visual-perception system, Small Struct. 1 (2020) 2000029.
[15] C. Han, X. Han, J. Han, M. He, S. Peng, C. Zhang, X. Liu, J. Gou, J. Wang, Light-stimulated synaptic transistor with high PPF feature for artificial visual perception system application, Adv. Funct. Mater. 32 (2022) 2113053.
[16] W. Xu, H. Cho, Y.H. Kim, Y.T. Kim, C. Wolf, C.G. Park, T.W. Lee, Organometal halide perovskite artificial synapses, Adv. Mater. 28 (2016) 5916–5922.
[17] R.A. John, N. Yantara, Y.F. Ng, G. Narasimman, E. Mosconi, D. Meggiolaro, M. R. Kulkarni, P.K. Gopalakrishnan, C.A. Nguyen, F. De Angelis, S.G. Mhaisalkar, A. Basu, N. Mathews, Ionotronic halide perovskite drift-diffusive synapses for low-power neuromorphic computation, Adv. Mater. 30 (2018) e1805454.
[18] Z. Xue, Y. Xu, C. Jin, Y. Liang, Z. Cai, J. Sun, Halide perovskite photoelectric artificial synapses: materials, devices, and applications, Nanoscale 15 (2023) 4653–4668.
[19] J.J. de Boer, B. Ehrler, Scalable microscale artificial synapses of lead halide perovskite with femtojoule energy consumption, ACS Energy Lett. (2024) 5787–5794.
[20] P. Zhao, M. Cui, Y. Li, J. Lao, C. Jiang, C. Luo, B. Tian, H. Lin, H. Peng, C.-G. Duan, Self-powered optoelectronic artificial synapses based on a lead-free perovskite film for artificial visual perception systems, J. Mater. Chem. C. 11 (2023) 6212–6219.
[21] Y. Lee, J. Kwon, E. Hwang, C.-H. Ra, W.J. Yoo, J.-H. Ahn, J.H. Park, J.H. Cho, High-performance perovskite–graphene hybrid photodetector, Adv. Mater. 27 (2015) 41–46.
[22] Q. Dong, Y. Fang, Y. Shao, P. Mulligan, J. Qiu, L. Cao, J. Huang, Electron-hole diffusion lengths > 175 μm in solution-grown CH3NH3PbI3 single crystals, Science 347 (2015) 967–970.
[23] Z. Xiao, J. Huang, Energy-efficient hybrid perovskite memristors and synaptic devices, Adv. Electron. Mater. 2 (2016).
[24] Y. Wang, Z. Lv, Q. Liao, H. Shan, J. Chen, Y. Zhou, L. Zhou, X. Chen, V.A.L. Roy, Z. Wang, Z. Xu, Y.J. Zeng, S.T. Han, Synergies of electrochemical metallization and valance change in all-inorganic perovskite quantum dots for resistive switching, Adv. Mater. 30 (2018) e1800327.
[25] S. Hong, S.H. Choi, J. Park, H. Yoo, J.Y. Oh, E. Hwang, D.H. Yoon, S. Kim, Sensory adaptation and neuromorphic phototransistors based on CsPb(Br(1-x)I(x))(3) perovskite and MoS(2) hybrid structure, ACS Nano 14 (2020) 9796–9806.
[26] L. Yang, M. Singh, S.W. Shen, K.Y. Chih, S.W. Liu, C.I. Wu, C.W. Chu, H.W. Lin, Transparent and flexible inorganic perovskite photonic artificial synapses with dual-mode operation, Adv. Funct. Mater. 31 (2020).
[27] Y. Sun, L. Qian, D. Xie, Y. Lin, M. Sun, W. Li, L. Ding, T. Ren, T. Palacios, Photoelectric synaptic plasticity realized by 2D perovskite, Adv. Funct. Mater. 29 (2019).
[28] J.-Y. Mao, Z. Zheng, Z.-Y. Xiong, P. Huang, G.-L. Ding, R. Wang, Z.-P. Wang, J.-Q. Yang, Y. Zhou, T. Zhai, S.-T. Han, Lead-free monocrystalline perovskite resistive switching device for temporal information processing, Nano Energy 71 (2020).
[29] J. Lao, W. Xu, C. Jiang, N. Zhong, B. Tian, H. Lin, C. Luo, J. Travas-sejdic, H. Peng, C.-G. Duan, An air-stable artificial synapse based on a lead-free double perovskite Cs2AgBiBr6 film for neuromorphic computing, J. Mater. Chem. C. 9 (2021) 5706–5712.
[30] Y. Park, M.-K. Kim, J.-S. Lee, 2D layered metal-halide perovskite/oxide semiconductor-based broadband optoelectronic synaptic transistors with long-term visual memory, J. Mater. Chem. C. 9 (2021) 1429–1436.
[31] Y.H. Lee, D.H. Kim, C. Wu, T.W. Kim, Memristive devices with a large memory margin based on nanocrystalline organic-inorganic hybrid CH3NH3PbBr3 perovskite active layer, Org. Electron. 62 (2018) 412–418.
[32] Y. Park, J.S. Lee, Metal Halide Perovskite-Based Memristors for Emerging Memory Applications, J. Phys. Chem. Lett. 13 (2022) 5638–5647.
[33] B. Ku, B. Koo, A.S. Sokolov, M.J. Ko, C. Choi, Two-terminal artificial synapse with hybrid organic–inorganic perovskite (CH3NH3)PbI3 and low operating power energy (~47 fJ/μm2), J. Alloy. Compd. 833 (2020).
[34] J.C. Pérez-Martínez, M. Berruet, C. Gonzales, S. Salehpour, A. Bahari, B. Arredondo, A. Guerrero, Role of metal contacts on halide perovskite memristors, Adv. Funct. Mater. 33 (2023).
[35] Metal-Semiconductor Contacts, in: Physics of Semiconductor Devices, 2006, pp. 134-196.
[36] H. Zhou, Q. Chen, G. Li, S. Luo, T.-b Song, H.-S. Duan, Z. Hong, J. You, Y. Liu, Y. Yang, Interface engineering of highly efficient perovskite solar cells, Science 345 (2014) 542–546.
[37] Y. Yun, D. Vidyasagar, M. Lee, O.Y. Gong, J. Jung, H.-S. Jung, D.H. Kim, S. Lee, Intermediate phase-free process for methylammonium lead iodide thin film for high-efficiency perovskite solar cells, Adv. Sci. 8 (2021) 2102492.
[38] J. Ye, M.M. Byranvand, C.O. Martínez, R.L.Z. Hoye, M. Saliba, L. Polavarapu, Defect passivation in lead-halide perovskite nanocrystals and thin films: toward efficient LEDs and Solar Cells, Angew. Chem. Int. Ed. 60 (2021) 21636–21660.
[39] S.-Y. Kim, H.-C. Lee, Y. Nam, Y. Yun, S.-H. Lee, D.H. Kim, J.H. Noh, J.-H. Lee, D.-H. Kim, S. Lee, Y.-W. Heo, Ternary diagrams of the phase, optical bandgap energy and photoluminescence of mixed-halide perovskites, Acta Mater. 181 (2019) 460–469.
[40] G. Grancini, A.R. Srimath Kandada, J.M. Frost, A.J. Barker, M. De Bastiani, M. Gandini, S. Marras, G. Lanzani, A. Walsh, A. Petrozza, Role of microstructure in the electron-hole interaction of hybrid lead-halide perovskites, Nat. Photonics 9 (2015) 695–701.
[41] C. Gonzales, A. Guerrero, Mechanistic and kinetic analysis of perovskite memristors with buffer layers: the case of a two-step set process, J. Phys. Chem. Lett. 14 (2023) 1395–1402.
[42] M.H. Lee, K.M. Kim, G.H. Kim, J.Y. Seok, S.J. Song, J.H. Yoon, C.S. Hwang, Publisher's Note: "Study on the electrical conduction mechanism of bipolar resistive switching TiO2 thin films using impedance spectroscopy" [Appl. Phys. Lett. 96, 152909 (2010)], Appl. Phys. Lett. 96 (2010) 219901.
[43] R. Waser, R. Dittmann, G. Staikov, K. Szot, Redox-based resistive switching memories – nanoionic mechanisms, prospects, and challenges, Adv. Mater. 21 (2009) 2632–2663.
[44] Y. Sun, M. Tai, C. Song, Z. Wang, J. Yin, F. Li, H. Wu, F. Zeng, H. Lin, F. Pan, Competition between metallic and vacancy defect conductive filaments in a CH3NH3PbI3-based memory device, J. Phys. Chem. C. 122 (2018) 6431–6436.
[45] B. Hwang, C. Gu, D. Lee, J.S. Lee, Effect of halide-mixing on the switching behaviors of organic-inorganic hybrid perovskite memory, Sci. Rep. 7 (2017) 43794.
[46] G. Milano, M. Aono, L. Boarino, U. Celano, T. Hasegawa, M. Kozicki, S. Majumdar, M. Menghini, E. Miranda, C. Ricciardi, S. Tappertzhofen, K. Terabe, I. Valov, Quantum conductance in memristive devices: fundamentals, developments, and applications, Adv. Mater. 34 (2022) e2201248.
[47] Y. Sun, C. Song, J. Yin, X. Chen, Q. Wan, F. Zeng, F. Pan, Guiding the growth of a conductive filament by nanoindentation to improve resistive switching, ACS Appl. Mater. Interfaces 9 (2017) 34064–34070.
[48] H. Lee, Y.K. Lee, E. Hwang, J.Y. Park, Enhanced surface plasmon effect of Ag/TiO2 nanodiodes on internal photoemission, J. Phys. Chem. C. 118 (2014) 5650–5656.
[49] D. Vidyasagar, Y.H. Yun, S. Shin, J. Jung, W. Park, J.W. Lee, G.S. Han, C. Ko, S. Lee, In-Situ Nano-Auger Probe of Chloride-Ions during CH(3)NH(3)PbI(3-x)Cl(x) Perovskite Formation, Mater. (Basel) 14 (2021).
[50] W. Rehman, D.P. McMeekin, J.B. Patel, R.L. Milot, M.B. Johnston, H.J. Snaith, L. M. Herz, Photovoltaic mixed-cation lead mixed-halide perovskites: links between crystallinity, photo-stability and electronic properties, Energy Environ. Sci. 10 (2017) 361–369.
[51] J. Jung, Y. Yun, S.W. Yang, H.G. Oh, A.Y. Jeon, Y. Nam, Y.-W. Heo, W.-S. Chae, S. Lee, Ternary diagrams of phase, stability, and optical properties of cesium lead mixed-halide perovskites, Acta Mater. 246 (2023) 118661.

[52] Y. Yun, H. Cho, J. Jung, S.W. Yang, D. Vidyasagar, R.K. Gunasekaran, S. Lee, High-performance self-powered color filter-free blue photodetector based on wide-bandgap halide perovskites, J. Mater. Sci. Technol. 152 (2023) 100–108.
[53] W. Tian, R. Cui, J. Leng, J. Liu, Y. Li, C. Zhao, J. Zhang, W. Deng, T. Lian, S. Jin, Limiting perovskite solar cell performance by heterogeneous carrier extraction, Angew. Chem. Int. Ed. 55 (2016) 13067–13071.
[54] M. Yang, Y. Zhou, Y. Zeng, C.-S. Jiang, N.P. Padture, K. Zhu, Square-centimeter solution-processed planar CH3NH3PbI3 perovskite solar cells with efficiency exceeding 15, Adv. Mater. 27 (2015) 6363–6370.
[55] Z. Gong, W. Zhao, K. Guan, P. Rao, Q. Zeng, J. Liu, Z. Feng, Influence of grain boundary and grain size on the mechanical properties of polycrystalline ceramics: Grain-scale simulations, J. Am. Ceram. Soc. 103 (2020) 5900–5913.
[56] T.S. Sherkar, C. Momblona, L. Gil-Escrig, J. Avila, M. Sessolo, H.J. Bolink, L.J. A. Koster, Recombination in perovskite solar cells: significance of grain boundaries, interface traps, and defect ions, ACS Energy Lett. 2 (2017) 1214–1222.
[57] H. Yu, J. Gong, H. Wei, W. Huang, W. Xu, Mixed-halide perovskite for ultrasensitive two-terminal artificial synaptic devices, Mater. Chem. Front. 3 (2019) 941–947.